VIBRATION AND NOISE ALLEVIATION IN ROTORCRAFT USING ON-BLADE CONTROL IMPLEMENTED BY MICROFLAPS

Peretz P. Friedmann
François-Xavier Bagnoud
Professor of Aerospace Engineering
peretzf@umich.edu

Ashwani K. Padthe
Postdoctoral Researcher
akpadthe@umich.edu

Department of Aerospace Engineering
University of Michigan, Ann Arbor, Michigan

Abstract

The effectiveness of on-blade control for vibration and noise alleviation in rotorcraft is examined in detail. The on-blade control is implemented by two sliding microflap configurations. The first was a dual microflap configuration, and the second one was a five microflap configuration. First, vibration and noise alleviation is examined under blade vortex interaction (BVI) conditions in descending flight at $\mu = 0.15$. Vibration reduction at high advance ratio at $\mu = 0.30$ is also examined. The performance of the microflaps were also compared to a dual plain flap configuration. Several important issues associated with this on-blade control problem are considered, such as: (1) simultaneous vibration and noise reduction, and (2) actuator saturation when the on-blade control is implemented by multiple control surfaces. The study indicates that microflaps are effective on-blade control devices for vibration and noise alleviation. Their potential for vibration and noise control compares favorably with on-blade control implemented by conventional partial span trailing edge flaps.

Nomenclature

b	Rotor blade semi-chord $= \frac{c_b}{2}$
c_b	Rotor blade chord
$\mathbf{C}_0, \mathbf{C}_1, ..., \mathbf{C}_{n+1}$	Rational function coefficient matrices
C_d	Drag coefficient
C_{df}	Fuselage drag coefficient
C_{hm}	Hinge moment coefficient
C_l	Lift coefficient
C_m	Moment coefficient
C_W	Helicopter weight coefficient
$\mathbf{D}, \mathbf{E}, \mathbf{R}$	Matrices defined in the RFA model
e	Blade root offset from center of rotation
f	Equivalent flat plate area of the fuselage
$\mathbf{f}$	Generalized load column matrix
$\mathbf{G}$	Laplace transform of $\mathbf{f}(\bar{t})U(\bar{t})$
$\mathbf{h}$	Generalized motion column matrix
$\mathbf{H}$	Laplace transform of $\mathbf{h}(\bar{t})$
k	Reduced frequency $= 2\pi\nu b/U$
L_b	Blade length
M	Mach number
M_b	Blade mass
N_b	Number of rotor blades
n_L	Number of lag terms
P_R	Average rotor power
$\mathbf{Q}$	Aerodynamic transfer function matrix
$\tilde{\mathbf{Q}}$	Approximation of $\mathbf{Q}$
R	Rotor blade radius
s	Laplace variable
$\bar{s}$	Nondim. Laplace variable $= sb/U$
$\mathbf{T}$	Sensitivity matrix relating control input to the plant output
t	Time
$\bar{t}$	Reduced time $= \frac{1}{b}\int_0^t U(\tau)d\tau$
$U(t)$	Freestream velocity, time-dependent
$\mathbf{u}$	control input vector
W_0, W_1	Generalized airfoil motions
X_A	Offset between the aerodynamic center and the elastic axis
X_{Ib}	Offset of the blade cross-sectional center of mass from the elastic axis

X_{FA}, Z_{FA}	Longitudinal and vertical offsets between rotor hub and helicopter aerodynamic center
X_{FC}, Z_{FC}	Longitudinal and vertical offsets between rotor hub and helicopter center of gravity
$\mathbf{x}(t)$	Aerodynamic state vector
$\mathbf{z}$	Plant output vector
α	Airfoil angle of attack
α_R	Rotor shaft angle
γ	Lock number
γ_n	Rational approximant poles
δ_f	Flap deflection
δ_{Nc}, δ_{Ns}	N/rev cosine and sine amplitudes of δ_f,
ϕ_R	Lateral roll angle
μ	Advance ratio
θ_0	Collective pitch
θ_{0t}	Tail rotor pitch angle
θ_{1c}, θ_{1s}	cyclic pitch components
θ_{pt}	Blade pretwist distribution
σ	Rotor solidity
$\omega_F, \omega_L, \omega_T$	Blade flap, lag and torsional natural frequencies
Ω	Rotor angular speed
ψ	Azimuth angle

1 Introduction and Background

Vibrations and noise have been major issues in rotorcraft. High levels of vibration and noise at low-speed descending flight conditions are attributed to blade-vortex interaction (BVI). During the last three decades, several active control approaches, such as the higher harmonic control (HHC) [1,2], individual blade control (IBC) [3, 4], and the actively controlled conventional plain trailing-edge flaps (ACF) [5–7] have been established as effective means for BVI vibration and noise reduction in rotorcraft. As indicated by the studies presented in Refs. 2, 5, 7, BVI noise reduction is often accompanied by increased vibration levels and vice versa. Although both vibrations and noise are caused by the BVI phenomena, the harmonic control inputs required for noise reduction are different from those needed for vibration reduction. Thus, reducing both BVI noise and vibrations simultaneously is challenging. Simultaneous reduction of noise and vibrations was systematically studied and demonstrated for the first time in Ref. 5 using a dual active trailing-edge servo flap configuration. A reduction of approximately 5 dB on the advancing side noise combined with a 40% reduction in the vertical hub shear was achieved.

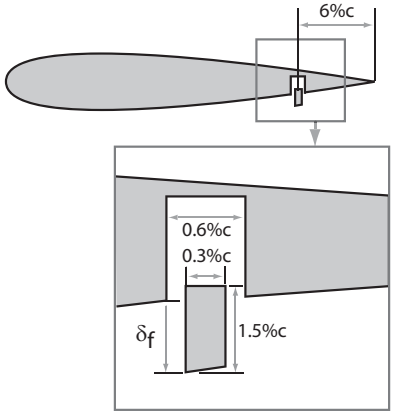

Figure 1: An oscillating microflap configuration used for active control studies.

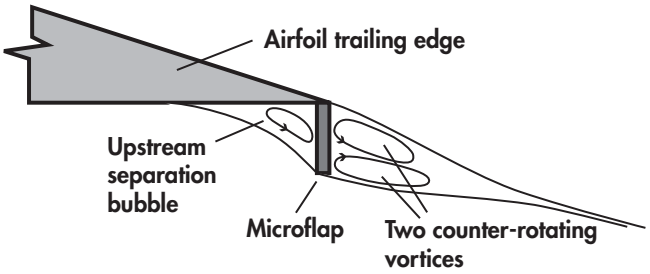

Figure 2: An illustration of the Gurney flap.

Recently the microflap, shown in Fig. 1, which is a deployable Gurney flap with a size of 1-3% of the blade chord and located near the trailing-edge of the airfoil, has emerged as a promising device for on-blade control of vibration and noise in helicopters [8–11]. One of the earliest experimental studies on aerodynamics of a Gurney flap was conducted by Liebeck [12], who hypothesized that the Gurney flap caused the flow to turn around the trailing edge resulting in the formation of two counter-rotating vortices behind the Gurney flap, as depicted in Fig. 2. The turning of the flow shifts the trailing edge stagnation point to the bottom edge of the microflap thus changing the Kutta condition and increasing the effective camber of the airfoil. Several experimental studies have shown that the Gurney flap is capable of increasing the maximum lift coefficient of an airfoil by up to 30% [12–15]. The lift enhancing capabilities of the Gurney flap have also been confirmed using computational fluid dynamics (CFD) simulations [14, 16].

Due to its small size, the microflap has the potential for high bandwidth active control with low actuation power requirements and minimal impact on the blade structure when compared to conventional control surfaces. Furthermore, the small size of microflaps may facilitate their retrofitting on existing helicopter rotor blades with relatively few modifica-

tions. The microflap has been studied for active control applications in fixed wing aircraft such as flutter suppression of high aspect ratio flexible wings [17] and wing trailing edge vortex alleviation [18, 19]. It was found that the deployable microflaps can increase flutter speed of a highly flexible wing by up to 22% [17]. The potential of microflaps with application to active load control in wind turbine blades has been explored computationally and experimentally on representative wind turbine airfoil sections [16, 20].

Several computational and experimental studies have considered microflaps for rotorcraft performance enhancement [21, 22]. A relatively simple deployment schedule where the microflaps are deployed primarily on retreating side of the disk was used in Ref. 21. The maximum thrust of the rotor was enhanced by 10% using microflaps with a 1% of chord height distributed along the entire blade span. Recently, microflaps were studied extensively for vibration and noise reduction in helicopters [8, 9]. In Ref. 8, a CFD based reduced order model (ROM) capable of reproducing with very good accuracy the unsteady, nonlinear aerodynamics of oscillating microflaps was developed. Such a ROM is a critical prerequisite for conducting closed-loop active control studies for vibration and noise reduction employing microflaps. Active vibration and noise reduction using on blade control implemented by microflaps has been explored recently [10, 11] using an adaptive higher harmonic control algorithm [23].

The issue of actuator saturation was also explored in Refs. [10, 11], where four different approaches for dealing with actuator saturation were considered, as described below:

1. Truncation (TR) which implies clipping the optimal flap deflection, as determined by the HHC controller, whenever it exceeds the saturation limits.

2. Scaling (SC) which consists of a uniform reduction of the optimal flap deflection such that it does not exceed the saturation limits.

3. Auto-weighting (AW) which is an iterative adjustment of the control activity weighting matrix in the HHC algorithm such that the flap deflection is properly constrained.

4. Optimization (OPT) approach where constraints, formulated as inequality constraints on the deflections of the control surface, are combined with the quadratic cost function in the HHC algorithm resulting in a constrained nonlinear optimization problem.

The first three approaches TR, SC and AW involve *a posteriori* modification of the optimal control inputs generated by the HHC algorithm, whereas the fourth approach OPT consists of *a priori* modification of the HHC algorithm to account for the saturation limits. In Refs. [10, 11], it was shown that the TR and SC approaches were ineffective and produced very substantial degradation in controller performance. The AW approach provided good performance, however its iterative nature increases the computational cost. The OPT approach was the best, it produces excellent performance at low computational cost. Furthermore, it is ideally suited for on blade control implemented by multiple control surfaces.

The overall objective of the current paper is to demonstrate the effectiveness of on blade control implemented by microflaps for vibration and BVI noise reduction, including the effects of actuator saturation. The specific objectives of the paper are:

1. Demonstrate the potential of two microflap configurations for on blade control of vibration and BVI noise, including simultaneous vibration and noise reduction on a representative rotor configuration.

2. Compare the effectiveness of conventional partial span trailing edge flaps with microflaps for on blade control.

3. Demonstrate the effectiveness of the OPT approach for handling actuator saturation for on blade control of noise and vibration.

4. Identify an improved strategy for simultaneous alleviation of vibration and noise using active control.

2 A CFD Based Reduced Order Aerodynamic Model

The complex nonlinear structure of viscous flow behind the microflap requires a CFD based approach for the accurate treatment of microflap aerodynamics. Although various CFD tools have been used to determine the aerodynamic characteristics of a Gurney flap or microflap with reasonable accuracy, the computational costs of coupling CFD solvers directly with rotorcraft simulation codes are prohibitive when conducting parametric trend studies involving active control. This obstacle has been overcome by a nonlinear CFD based reduced-order aerodynamic model developed in Ref. 8 that has been shown to be accurate, efficient, and suitable for combination with comprehensive rotorcraft codes. The reduced-order model (ROM) is obtained by using a compressible unsteady Reynolds-Averaged Navier-Stokes (RANS)

CFD solver to generate frequency domain aerodynamic response to basic motions. Subsequently, the frequency domain loads are converted to the time-domain using the Rational Function Approximation (RFA) approach.

The RFA approach has been used to generate time domain unsteady aerodynamic loads for wing sections (i.e. two-dimensional) for both fixed wing [24] and rotary wing applications [25]. The model developed in Ref. 25 was aimed at generating the unsteady cross sectional loads for an airfoil/trailing edge flap combination, representing the cross section of the blade where a control surface is present. The model accounts for compressibility and variations in oncoming flow. In the original RFA model the cross sectional aerodynamic loads were obtained in the frequency domain using a doublet lattice unsteady potential flow solver. Subsequently a state-space formulation combined with the RFA approach was used to convert the loads to the time domain.

The new CFD based ROM also relies on the RFA approach and therefore it is denoted CFD+RFA model. It was developed in Refs. 8 and 26 which contain detailed descriptions of the model. The essential features of the model are summarized in Fig. 3. The airfoil and the control surfaces can undergo four generalized motions, shown in the figure. A CFD code (CFD++) is used to generate the frequency domain information for the airfoil/flap or airfoil/microflap configuration for the range of frequencies and helicopter operating conditions for which the ROM is expected to be used. The vector $\mathbf{h}$ represents the generalized motions that yield the vector of cross sectional frequency domain loads f. For the case of the plain flap shown in Fig. 3 the vector $\mathbf{f}$ contains the lift coefficient C_l, the moment coefficient C_m , the hinge moment coefficient C_{hm} and the drag coefficient C_d. For the microflap only three quantities are used because the hinge moment is negligible. The RFA approach is used to convert the frequency domain loads into the time domain using the Laplace transform.

The final state space representation relating the time domain generalized motions $\mathbf{h}(t)$ to the generalized loads $\mathbf{f}(t)$ is shown in the block at the bottom of Fig. 3, where the vector $\mathbf{x}(t)$ represents the vector of augmented aerodynamic states. In the original version of the RFA approach the matrices $\mathbf{R}, \mathbf{E}, \mathbf{C}_0$, and $\mathbf{C}_1$ associated with this approach were constant. However, in the CFD+RFA model these matrices are now functions of the Mach number M, the effective angle of attack α and the flap deflection δ_f. This modification of the original approach resembles the gain scheduling used in the design of nonlinear control systems.

The CFD++ code is used to generate the frequency domain data required for constructing the ROM [27,28], this modern commercially available code solves the compressible unsteady RANS equations. It uses a unified grid methodology that can handle a variety of structured, unstructured, multi-block meshes and cell types, including patched and overset grid features. Spatial discretization is based on a second order multi-dimensional Total Variation Diminishing (TVD) scheme. For temporal scheme an implicit algorithm with dual time-stepping is employed to perform time-dependent flow simulations, with multigrid convergence acceleration. Various turbulence models are available in CFD++ and the Spalart-Allmaras model is used in the current study, assuming a fully turbulent boundary layer.

The microflap shown in Fig. 1 was selected as the most suitable configuration [8]. The overall computational domain which contains approximately 90,000 grid points is shown in Fig. 4(a). The grids used for the microflap are shown in Fig. 4(b) and the grids for the plain flap are depicted in Fig. 4(c).

The CFD grids for the microflap or plain flap configurations are generated using the overset grid approach, a convenient method for modeling complex geometries and moving components with large relative motions. The grids are clustered at the airfoil wall boundaries such that the dimensionless distance y^+ of the first grid point off the wall is less than 1, and the equations are solved directly to the walls without assuming wall functions. Extensive verification of the CFD+RFA model predictions when compared to direct CFD calculations can be found in Ref. 8, for a wide range of flow conditions and unsteady microflap or plain flap deflections.

3 The Comprehensive Rotorcraft Aeroelastic Analysis Code

Active control simulations with the microflap are performed using a comprehensive rotorcraft aeroelastic code AVINOR which was validated in previous studies [5, 29]. The CFD+RFA aerodynamic model described earlier was incorporated into AVINOR and is employed for modeling the two-dimensional aerodynamic effect of the microflaps and plain trailing-edge flaps. The principal ingredients of the AVINOR code are concisely summarized next.

3.1 Structural dynamic model

The structural dynamic model used in this study consists of a four-bladed hingeless rotor, with fully coupled flap-lag-torsional dynamics for each blade. The structural dynamic model is geometrically nonlinear, due to moderate blade deflections. The struc-

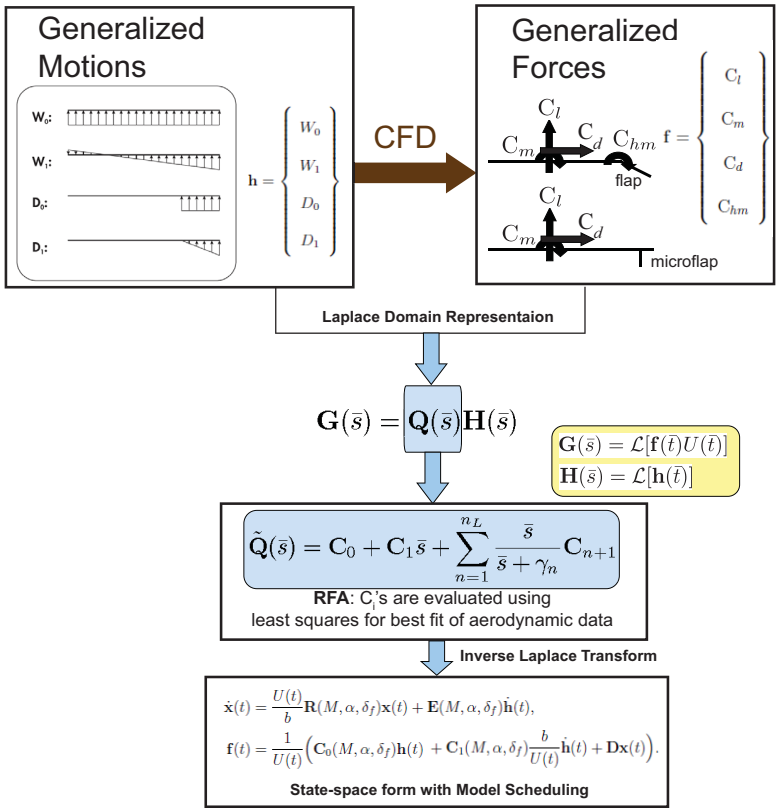

Figure 3: A schematic description of the CFD based RFA model.

tural equations of motion are discretized using the global Galerkin method, based upon the free vibration modes of the rotating blade. The dynamics of the blade are represented by three flap, two lead-lag, and two torsional modes. Free vibration modes of the blade were obtained using the first nine exact non-rotating modes of a uniform cantilevered beam. The effect of control surfaces such as the trailing-edge plain flap or the microflap on the structural properties of the blade were neglected. Thus, the control surfaces influence the blade behavior only through their effect on the aerodynamic and inertial loads.

3.2 Aerodynamic model

The blade/flap or blade/microflap sectional aerodynamic loads for attached flow are calculated using the CFD+RFA model described earlier. This model provides cross-sectional unsteady lift, moment, and drag for both plain flap and microflap configurations. The RFA model is linked to a free wake model described in Refs. 5 that yields a spanwise and azimuthally varying inflow distribution. For separated flow regime, the aerodynamic loads are calculated using the ONERA dynamic stall model [5].

3.3 Coupled aeroelastic response/trim solution

The vibratory hub shears and moments are obtained from the integration of the distributed inertial and aerodynamic loads over the entire blade span in the rotating frame. Subsequently, the loads are transformed to the hub-fixed non-rotating system, and the contributions from the individual blades are combined. In this process, the blades are assumed to be identical. This process yields the N_b/rev components, which are the dominant components of the hub shears and moments.

The combined structural and aerodynamic equations are represented by a system of coupled ordinary differential equations with periodic coefficients in state-variable form. The trim employed is a propulsive trim procedure where three force equations (longitudinal, lateral, and vertical) and three moment equations (roll, pitch, and yaw) corresponding to a helicopter in free flight are enforced. A simplified tail rotor model, based on uniform inflow and blade element theory, is used. The six trim variables are the rotor shaft angle α_R, the collective pitch θ_0, the cyclic pitch θ_{1s} and θ_{1c}, the tail rotor constant pitch θ_{0t}, and lateral roll angle ϕ_R. The coupled trim/aeroelastic equations are solved in time using the ODE solver DDE-ABM, which is a predictor-corrector based Adams-

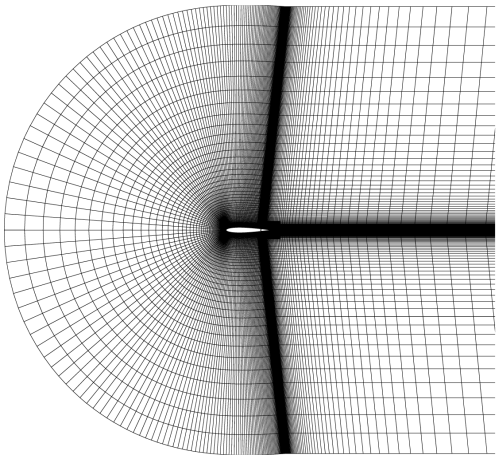

(a) Grid overview

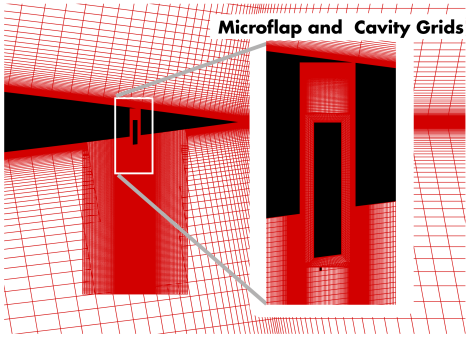

(b) Close-up grid for microflap

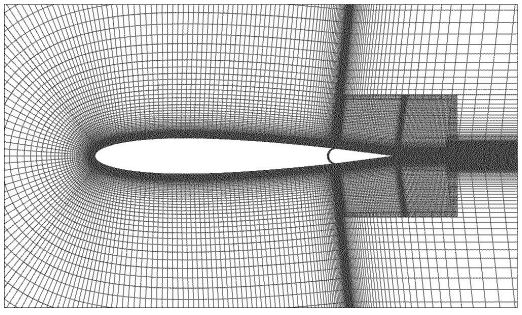

(c) Close-up grid for plain flap

Figure 4: Grids used for CFD simulations.

Bashforth differential system solver.

3.4 Acoustic model

The acoustic calculations are based on a modified version of the WOPWOP code, where helicopter noise is obtained from the Ffowcs-Williams Hawkings equation with the quadrupole term neglected [30]. The version of WOPWOP used in the code was modified to account for a fully flexible blade model that is compatible with the structural dynamic model described earlier. In previous studies [5, 31], the chordwise pressure distribution on the surface of the blade, a required input to the acoustic computations, was obtained using an extended RFA approach. The extended RFA approach used frequency domain pressure data obtained from the doublet lattice flow solver, described in detail in Ref. 31. Generating the extended RFA models using CFD based pressure distribution data is computationally expensive. To reduce the cost the blade pressure distributions are obtained from an approximate velocity superposition method [32]. Using potential flow the pressure distribution on the surface of the airfoil is related to the local velocity distribution that is assumed to result from three independent contributions

$$c_p = \left(\frac{v}{V} \pm \frac{\Delta v}{V} \pm \frac{\Delta v_a}{V} \right)^2 \tag{1}$$

where the velocity ratios $\frac{v}{V}$, $\frac{\Delta v}{V}$, and $\frac{\Delta v_a}{V}$ are contributions due to airfoil thickness, camber, and angle of attack, respectively. The signs in Eq. 1 are positive for the upper surface and negative for the lower surface of the airfoil. For the symmetric NACA 0012 airfoil used in the study, $\frac{\Delta v}{V} = 0$, and the values of the other two components are found from the approach described in Ref. 32. Since this approach is based on the potential flow theory it is not quite compatible with the CFD based RFA model. However, it represents an acceptable approximation because the lift coefficients from which the pressure distributions are obtained, are based on the CFD+RFA model that accounts for compressibility, viscosity, and unsteady effects.

3.5 The Higher Harmonic Control Algorithm

Active control of vibration and noise is implemented using the HHC algorithm used extensively for active control of vibration and noise in rotorcraft [5,23]. The algorithm is based on the assumption that the helicopter can be represented by a linear model relating the output of interest $\mathbf{z}$ to the control input

$\mathbf{u}$. The measurement of the plant output and update of the control input are performed at specific times $t_k = k\tau$, where τ is the time interval between updates during which the plant output reaches a steady state. In actual implementation of the algorithm, this time interval may be one or more revolutions. A schematic of the HHC architecture implemented on a helicopter is shown in Fig. 5. The disturbance $\mathbf{w}$ represents the

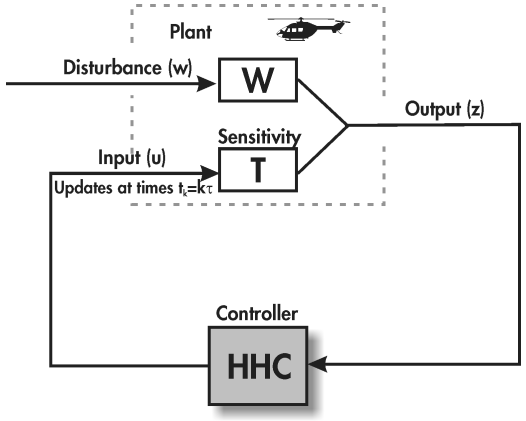

Figure 5: Higher harmonic control architecture

helicopter operating condition. The output vector at the k^{th} time step is given by

$$\mathbf{z}_k = \mathbf{T}\mathbf{u}_k + \mathbf{W}\mathbf{w} \tag{2}$$

where the sensitivity matrix $\mathbf{T}$ represents a linear approximation of the helicopter response to the control and is given by

$$\mathbf{T} = \frac{\partial \mathbf{z}}{\partial \mathbf{u}}. \tag{3}$$

At the initial condition, $k = 0$,

$$\mathbf{z}_0 = \mathbf{T}\mathbf{u}_0 + \mathbf{W}\mathbf{w}. \tag{4}$$

Subtracting Eq. (4) from Eq. (2) to eliminate the unknown $\mathbf{w}$ yields

$$\mathbf{z}_k = \mathbf{z}_0 + \mathbf{T}(\mathbf{u}_k - \mathbf{u}_0). \tag{5}$$

The controller is based on the minimization of a general quadratic cost function

$$J(\mathbf{z}_k, \mathbf{u}_k) = \mathbf{z}_k^{\mathrm{T}}\mathbf{Q}\mathbf{z}_k + 2\mathbf{z}_k^{\mathrm{T}}\mathbf{S}\mathbf{u}_k + \mathbf{u}_k^{\mathrm{T}}\mathbf{R}\mathbf{u}_k. \tag{6}$$

However, in most applications, the cross-weighting term in Eq. (6) is neglected thus the cost function reduces to

$$J(\mathbf{z}_k, \mathbf{u}_k) = \mathbf{z}_k^{\mathrm{T}}\mathbf{Q}\mathbf{z}_k + \mathbf{u}_k^{\mathrm{T}}\mathbf{R}\mathbf{u}_k. \tag{7}$$

The optimal control input is determined from the requirement

$$\frac{\partial J(\mathbf{z}_k, \mathbf{u}_k)}{\partial \mathbf{u}_k} = 0, \tag{8}$$

which yields the optimal control law $\mathbf{u}_{k,\mathrm{opt}}$, given by

$$\mathbf{u}_{k,\mathrm{opt}} = -(\mathbf{T}^{\mathrm{T}}\mathbf{Q}\mathbf{T} + \mathbf{R})^{-1}(\mathbf{T}^{\mathrm{T}}\mathbf{Q})(\mathbf{z}_0 - \mathbf{T}\mathbf{u}_0). \tag{9}$$

Combining Eqs. (5), (7) and (9), the minimum cost is

$$J(\mathbf{z}_k, \mathbf{u}_{k,\mathrm{opt}}) = (\mathbf{z}_0 - \mathbf{T}\mathbf{u}_0)^{\mathrm{T}} \left[\mathbf{Q} - (\mathbf{Q}\mathbf{T})\mathbf{D}^{-1}(\mathbf{T}^{\mathrm{T}}\mathbf{Q})\right](\mathbf{z}_0 - \mathbf{T}\mathbf{u}_0). \tag{10}$$

where

$$\mathbf{D} = \mathbf{T}^{\mathrm{T}}\mathbf{Q}\mathbf{T} + \mathbf{R} \tag{11}$$

This is a classical version of the HHC algorithm that yields an explicit relation for the optimal control input. Another version of the HHC algorithm where the sensitivity matrix $\mathbf{T}$ is updated using least-squares methods after every control update is known as the adaptive or recursive HHC [23]. In order to describe the adaptive HHC algorithm, relative output and input vectors are defined, $\Delta\mathbf{z}_k$, with length $2p$ and $\Delta\mathbf{u}_k$ with length $2m$ as

$$\Delta\mathbf{z}_k = \mathbf{z}_k - \mathbf{z}_{k-1}, \;\; \Delta\mathbf{u}_k = \mathbf{u}_k - \mathbf{u}_{k-1}, \tag{12}$$

and, $\Delta\mathbf{Z}_k$ of size $2p \times k$ and $\Delta\mathbf{U}_k$ of size $2m \times k$ as

$$\begin{aligned} \Delta\mathbf{Z}_k &= \left[\begin{array}{ccc} \Delta\mathbf{z}_1 & \cdots & \Delta\mathbf{z}_k \end{array}\right], \\ \Delta\mathbf{U}_k &= \left[\begin{array}{ccc} \Delta\mathbf{u}_1 & \cdots & \Delta\mathbf{u}_k \end{array}\right]. \end{aligned} \tag{13}$$

The relation between the successive updates of vibration levels $\mathbf{z}_k$ is

$$\mathbf{z}_k = \mathbf{z}_{k-1} + \mathbf{T}(\mathbf{u}_k - \mathbf{u}_{k-1}). \tag{14}$$

This can be represented in another form,

$$\Delta\mathbf{z}_k = \mathbf{T}\Delta\mathbf{u}_k. \tag{15}$$

Hence, it follows from Eqs. (15) and (13) that

$$\Delta\mathbf{Z}_k = \mathbf{T}\Delta\mathbf{U}_k. \tag{16}$$

Assuming $\Delta\mathbf{U}_k\Delta\mathbf{U}_k^{\mathrm{T}}$ is nonsingular, one can define

$$\mathbf{P}_k = (\Delta\mathbf{U}_k\Delta\mathbf{U}_k^{\mathrm{T}})^{-1}, \tag{17}$$

and from Eq. (16) the least squares estimate $\hat{\mathbf{T}}_{\mathrm{LS}_k}$ of $\mathbf{T}$ is given by

$$\hat{\mathbf{T}}_{\mathrm{LS}_k} = \Delta\mathbf{Z}_k\Delta\mathbf{U}_k^{\mathrm{T}}\mathbf{P}_k. \tag{18}$$

The recursive least squares method is used to iteratively update $\hat{\mathbf{T}}_{\mathrm{LS}_k}$ based on the past and current values of $\Delta\mathbf{z}_k$ and $\Delta\mathbf{u}_k$. The updated estimate $\hat{\mathbf{T}}_{\mathrm{LS}_k}$ is used at each control update step to calculate the optimal control input $\mathbf{u}_{k,\mathrm{opt}}$ given in Eq. 9. The adaptive HHC algorithm has been shown to perform better than the classical HHC when the model nonlinearities

are significant and the sensitivity matrix $\mathbf{T}$ is a poor approximation of the model [23].

3.6 Implementation of the HHC algorithm

In a 4-bladed rotor, the control input $\mathbf{u}_k$ is a combination of 2/rev, 3/rev, 4/rev, and 5/rev harmonic amplitudes of the control surface deflection:

$$\mathbf{u}_k = [\delta_{2c}, \delta_{2s}, ..., \delta_{5c}, \delta_{5s}]^T. \tag{19}$$

where the term 'control surface' is used to denote both the microflap or conventional plain trailing-edge flap. The total control surface deflection is given by

$$\delta(\psi, \mathbf{u}_k) = \sum_{N=2}^{5} \left[\delta_{Nc} \cos(N\psi) + \delta_{Ns} \sin(N\psi)\right]. \tag{20}$$

where the quantities δ_{Nc} and δ_{Ns} correspond to the cosine and sine components of the N/rev control input harmonic. When multiple control surfaces are used, the control surface deflections are given by

$$\delta_i(\psi, \mathbf{u}_k) = \sum_{N=2}^{5} \left[\delta_{Nci} \cos(N\psi) + \delta_{Nsi} \sin(N\psi)\right], \tag{21}$$

$$\tag{22}$$

where $i = 1, \ldots, N_\delta$ and N_δ is the total number of control surfaces. The control vector $\mathbf{u}_k$ is then given by

$$\begin{aligned}\mathbf{u}_k = [&\delta_{2c1}, \delta_{2s1}, ..., \delta_{5c1}, \delta_{5s1}, \ldots, \\ &\delta_{2cN_\delta}, \delta_{2sN_\delta}, ..., \delta_{5cN_\delta}, \delta_{5sN_\delta}]^T.\end{aligned} \tag{23}$$

For vibration reduction (VR) studies, the output vector $\mathbf{z}_k$ consists of 4/rev vibratory hub shears and moments:

$$\mathbf{z}_{\text{VR}} = \begin{bmatrix} F_{HX4} \\ F_{HY4} \\ F_{HZ4} \\ M_{HX4} \\ M_{HY4} \\ M_{HZ4} \end{bmatrix} \tag{24}$$

The weighting matrix $\mathbf{Q}$ in the cost function in Eq. 7 is a diagonal matrix. For vibration control, it is described by six weights corresponding to the three vibratory hub shears and the three vibratory hub moments. For BVI noise reduction (NR) studies, the output vector consists of the 6^{th}-17^{th} blade passage frequency harmonic components of the rotor noise, which represent the principal part of BVI noise, measured by a microphone installed on the skid or landing gear of the helicopter, and

$$\mathbf{z}_{\text{NR}} = \begin{bmatrix} N_{H06} \\ N_{H07} \\ N_{H08} \\ \vdots \\ N_{H17} \end{bmatrix} \tag{25}$$

For simultaneous vibration and noise reduction (SR) problems, a combined output vector is defined by

$$\mathbf{z}_{\text{SR}} = \left[\frac{\mathbf{z}_{\text{VR}}}{\mathbf{z}_{\text{NR}}}\right], \tag{26}$$

where the vector $\mathbf{z}_{\text{SR}}$ is simply a partitioned combination of the vibration and noise levels. The combined weighting matrix $\mathbf{Q}_{\text{SR}}$ is defined as

$$\mathbf{Q}_{\text{SR}} = \begin{bmatrix} (W_\alpha) \cdot [\mathbf{Q}_{\text{VR}}] & 0 \\ 0 & (1 - W_\alpha) \cdot [\mathbf{Q}_{\text{NR}}] \end{bmatrix}. \tag{27}$$

Where, W_α is a scalar factor used to adjust the relative weighting between noise and vibration as objectives for the controller. When $W_\alpha = 1$, the control effort is focused on vibration reduction, and when $W_\alpha = 0$, only noise is reduced by the controller. During approach to landing, BVI noise is the main priority, while vibration is the goal at cruise conditions. Therefore, in an actual implementation the weighting factor can be adjusted by the controller depending on the desired outcome. The weighting matrices $\mathbf{Q}_{\text{VR}}$ and $\mathbf{Q}_{\text{NR}}$ used for simultaneous noise and vibration reduction performed in this study are:

$$\mathbf{Q}_{\text{VR}} = \begin{bmatrix} 1 & 0 & 0 & 0 & 0 & 0 \\ 0 & 1 & 0 & 0 & 0 & 0 \\ 0 & 0 & 10 & 0 & 0 & 0 \\ 0 & 0 & 0 & 10 & 0 & 0 \\ 0 & 0 & 0 & 0 & 10 & 0 \\ 0 & 0 & 0 & 0 & 0 & 10 \end{bmatrix}, \tag{28}$$

and

$$\mathbf{Q}_{\text{NR}} = \begin{bmatrix} 100 & 0 & 0 & 0 & \ldots & \ldots & 0 \\ 0 & 100 & 0 & 0 & \ldots & \ldots & 0 \\ 0 & 0 & 100 & 0 & \ldots & \ldots & 0 \\ & & & \ddots & & & \\ 0 & \ldots & \ldots & 0 & 100 & 0 & 0 \\ 0 & \ldots & \ldots & 0 & 0 & 100 & 0 \\ 0 & \ldots & \ldots & 0 & 0 & 0 & 100 \end{bmatrix}. \tag{29}$$

3.7 Actuator Saturation

Most actuation devices used for on blade control of rotorcraft vibrations and noise are subject to amplitude saturation. Furthermore, the actuation am-

plitudes have to be limited so as to avoid undesirable interactions between the primary flight control system and the on blade controller. For a microflap the maximum deflection is constrained by its size, usually 1.5% of the chord. For a conventional trailing-edge flap the maximum deflection is set to 4°. As mentioned in the introduction four different approaches for implementing actuator saturation on the performance of the on blade controller have been examined recently [10, 11]. The approaches considered for actuator saturation are: truncation (TR), scaling (SC), auto-weighting (AW) and optimization (OPT).

Truncation: in this approach the unconstrained optimal control input is clipped whenever it exceeds the limiting amplitude, thus the control surface deflection is

$$\delta(\psi, \mathbf{u}_k) = \begin{cases} \delta(\psi, \mathbf{u}_k), & |\delta(\psi, \mathbf{u}_k)| < \delta_{\text{limit}} \\ \text{sgn}(\delta(\psi, \mathbf{u}_k)) \cdot \delta_{\text{limit}}, & |\delta(\psi, \mathbf{u}_k)| \geq \delta_{\text{limit}} \end{cases} \tag{30}$$

where δ_{limit} is the saturation limit on the control surface deflection.

Scaling: for this case the optimal control input is given by

$$\delta(\psi, \mathbf{u}_k) = \frac{\delta_{\text{limit}}}{\max(|\delta_{\text{opt}}(\psi, \mathbf{u}_k)|)} \cdot \delta_{\text{opt}}(\psi, \mathbf{u}_k), \tag{31}$$

where $\delta_{\text{opt}}(\psi, \mathbf{u}_k)$ is the optimal control input obtained using the HHC algorithm without the saturation constraints. Each harmonic component of the optimal control surface deflection is scaled by a common factor such that the maximum deflection is equal to the saturation limit.

Auto-weighting: in this case the control weighting matrix, $\mathbf{R}$ in Eq. (7), is updated so as to restrict the control surface deflection. The control weighting matrix $\mathbf{R}$ penalizes the control input and thus can be used to constrain the maximum control surface deflection. However, the value of $\mathbf{R}$ required to constrain the control input amplitude within the saturation limits is not known a priori. Hence, an iterative approach which adjusts the value of $\mathbf{R}$ is used. The weighting matrix $\mathbf{R}$ is represented as:

$$\mathbf{R} = c_{wu}\mathbf{I}. \tag{32}$$

where c_{wu} is a scalar and $\mathbf{I}$ is the identity matrix. In this approach all harmonic components of the control input vector are weighted equally. If the control surface deflection is overconstrained, the controller reduces the value of c_{wu}. If the control surface deflection is underconstrained, the controller increases the value of c_{wu}. A new optimal control is calculated using the updated value of c_{wu}, obtained as follows:

1. Set $c_{wu}^- = 0$ and $c_{wu}^+ = c_{\max}$.
2. Set $c_{wu} = \frac{1}{2}(c_{wu}^- + c_{wu}^+)$
3. Calculate a new optimal control input.

   If the flap deflection is properly constrained ($|\delta_{\max}| = \delta_{\text{limit}} \pm 5\%$), end the algorithm.

   If the flap deflection is underconstrained ($|\delta_{\max}| > \delta_{\text{limit}}$), set $c_{wu}^- = \frac{1}{2}(c_{wu}^- + c_{wu}^+)$. Return to step 2.

   If the flap deflection is overconstrained ($|\delta_{\max}| < \delta_{\text{limit}}$), set $c_{wu}^+ = \frac{1}{2}(c_{wu}^- + c_{wu}^+)$. Return to step 2.

This iterative procedure increases or decreases c_{wu} until the optimal control surface deflection converges to the desired deflection limits within a prescribed tolerance. The value of $c_{\max}$, specified in step 1, has to be guessed initially and it has to be greater than or equal to the optimum value of c_{wu} that properly constrains the control input. Choosing a very large value for $c_{\max}$ is not recommended since depending on the proximity of $c_{\max}$ to the optimum c_{wu}, the AW approach can take several iterations causing an increase in the computational costs. Furthermore, for the case of multiple control surfaces, the number of iterations required for all of them to be properly constrained can be quite high rendering the AW approach impractical. To avoid this situation the same value of c_{wu} is used for all the control surfaces.

Optimization: this approach is based on constrained nonlinear optimization techniques, and it overcomes the limitations associated with the previous approaches. Recall that the HHC algorithm is based on the minimization of a quadratic cost function, given by Eq. (7). The saturation limits can be combined with the minimization of the cost function to yield a constrained optimization problem:

$$\underset{\mathbf{u}_k}{\text{minimize}} \quad J(\mathbf{z}_k, \mathbf{u}_k) = \mathbf{z}_k^{\text{T}}\mathbf{Q}\mathbf{z}_k + \mathbf{u}_k^{\text{T}}\mathbf{R}\mathbf{u}_k, \tag{33}$$

$$\text{subject to} \quad |\delta_i(\psi, \mathbf{u}_k)| \leq \delta_{\text{limit}}, \quad i = 1, \ldots, N_\delta \tag{34}$$

where N_δ is the total number of control surfaces. The optimization problem given by Eqs. (33) and (34) is a nonlinear constrained optimization problem with a quadratic objective function and nonlinear inequality constraints, denoted as a Nonlinear Programming (NP) problem. Unlike the approaches described earlier, this approach involves direct modifications to the HHC algorithm to account for the presence of saturation in an *a priori* manner. The resulting optimal control input always satisfies the saturation limits irrespective of the values of $\mathbf{R}$ and $\mathbf{Q}$.

A NP method, Sequential Quadratic Programming (SQP) [33, 34], available in the FMINCON tool in MATLAB, is used to solve the optimization problem given by Eqs. (33) and (34). The SQP method

solves a quadratic programming subproblem based on a quadratic approximation of the Lagrangian function. A stand-alone application (a *.exe* file) capable of performing the optimization is generated using the *mcc -m* command in Matlab. Subsequently, this application is invoked from the AVINOR code, written in FORTRAN, in order to evaluate the optimum $\mathbf{u}_k$. The stand-alone application requires approximately 1 sec to run on a 2.53 GHz Intel Xeon processor in the case of a single control surface. Note that the nonlinear constraints described in Eq. (34) have to be satisfied for all values of the azimuth angle $\psi \in [0^\circ \quad 360^\circ]$. In actual numerical implementation, the nonlinear constraints are evaluated and enforced at every integer value of ψ over the range $[0^\circ \quad 360^\circ]$.

4 Results and Discussion

The results provided in this section were generated for a helicopter configuration resembling a full-scale four-bladed MBB BO-105 hingeless rotor. The rotor parameters are listed in Table 1. The rotor is trimmed using a propulsive trim procedure. All the values in the table (except C_W, γ, and σ) have been nondimensionalized using M_b, L_b, and $1/\Omega$ for mass, length and time, respectively. The mass and stiffness distributions are assumed to be constant along the span of the blade.

The acoustic environment in the vicinity of the helicopter is characterized by the noise decibel levels computed on a carpet plane located 1.15R beneath the rotor, shown in Fig. 6. Noise measured by a microphone located at the rear of the right landing skid is used as the feedback signal to the controller. The sharp trailing edge configuration, shown in Fig. 1, was chosen for the microflap. The microflap, 1.5%c in height, slides in and out of a cavity, located 6%c in front of the trailing edge of the airfoil.

Two different spanwise microflap configurations are considered for the simultaneous BVI noise and vibration reduction studies. The first is dual microflap configuration, shown in Figure 7(a). It consists of two microflaps each having a spanwise dimension of 0.06R centered at spanwise locations of 0.72R and 0.92R, respectively. The second configuration shown in Figure 7(b) consists of five microflaps with spanwise dimension of 0.05R each located adjacent to each other. Active control studies were also conducted using a 20%c conventional plain flap, shown in Fig. 8, implemented a dual flap configuration, shown in Fig. 9.

Table 1: Rotor parameters used for noise and vibration reduction studies.

Dimensional Rotor Data	
$R = 4.91$ m	
$M_b = 27.35$ kg	
$\Omega = 425$ RPM	
Nondimensional Rotor Data	
$N_b = 4$	$L_b = 1.0$
$c/R = 0.05498$	$\theta_{\text{tw}} = -8^\circ$
$e = 0$	
$X_A = 0$	$X_{Ib} = 0$
$\omega_F = 1.124, 3.40, 7.60$	$\omega_L = 0.732, 4.458$
$\omega_T = 3.17, 9.08$	
$\gamma = 5.5$	$\sigma = 0.07$
$\beta_p = 2.5^\circ$	
Helicopter Data	
$C_W = 0.005$	$fC_{df} = 0.031$
$X_{FA} = 0.0$	$Z_{FA} = 0.3$
$X_{FC} = 0.0$	$Z_{FC} = 0.3$

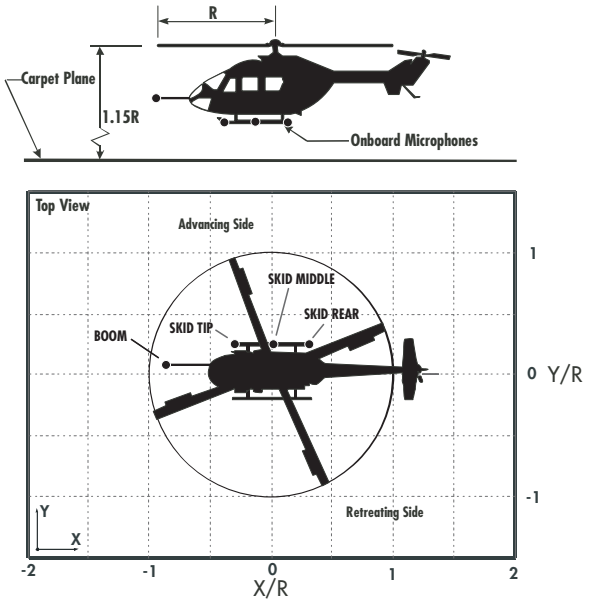

Figure 6: Microphone locations on and around the helicopter for noise measurements.

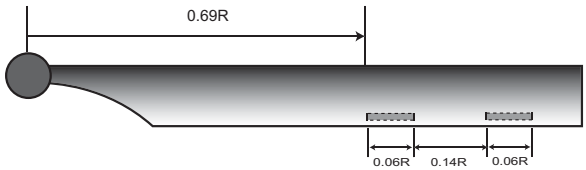

(a) Dual Microflap

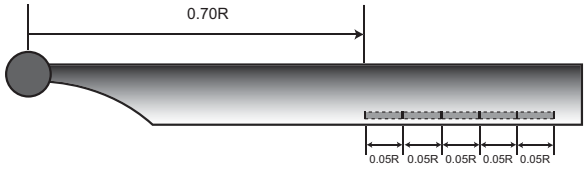

(b) Five Microflaps

Figure 7: Various spanwise configurations of the microflap on the rotor blade.

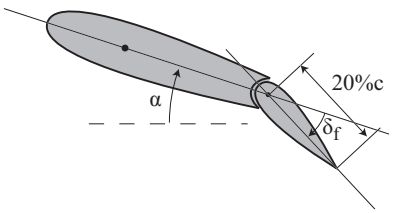

Figure 8: A 20%c conventional plain flap configuration.

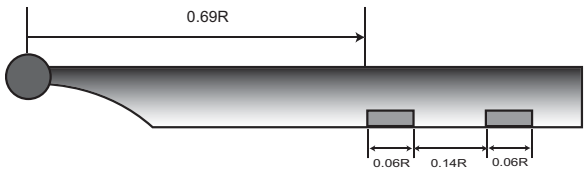

(a) Dual plain flap

Figure 9: Dual spanwise configuration of the 20%c plain flap on the rotor blade.

Table 2: Simultaneous vibration and noise reduction obtained using the dual microflap configuration for various values of the relative weighting parameter W_α.

W_α	% change in 4/rev vertical hub shear	dB change in right rear skid noise
0.1	16	-3.0
0.2	14	-2.5
0.3	-2	-2.4
0.4	-2	-2.3
0.5	-20	-1.8
0.6	-34	-1.6
0.7	-31	-1.3
0.8	-38	-0.3
0.9	-44	0.8

4.1 Simultaneous BVI noise and vibration reduction

Results presented in Ref. 35 indicate that BVI noise reduction using microflaps is often accompanied by increased vibration levels and vice versa. The feasibility of reducing both BVI noise and vibrations simultaneously using microflaps is explored in this paper. The adaptive HHC algorithm is employed for all the active control simulations. Simultaneous reduction studies are conducted using the dual and five microflap configurations under heavy BVI descending flight condition at an advance ratio $\mu = 0.15$ and a descent angle $\alpha_D = 6.5°$. Simulations are performed using various values of the relative weighting parameter W_α, in Eq. 27. Changes in the 4/rev vertical hub shear and the noise levels measured at the right rear skid location corresponding to various W_α values are given in Table 2 for the dual microflap configuration. The value of $W_\alpha = 0.6$ yields the best combination for simultaneous vibration and noise reduction and thus represents a Pareto optimal combination. Similar information is provided for the five-microflap configuration in Table 3. The best combination for simultaneous reductions of vibration and noise is obtained at $W_\alpha = 0.7$. Simultaneous vibration and noise reduction results for these optimal values of W_α are presented next.

Noise levels computed during simultaneous vibration and noise reduction using the dual and five microflap configurations are compared to the baseline noise levels in Fig. 10. The dual microflap configuration yields up to 2 dB noise reduction on both the advancing and retreating sides. The five microflap configuration yields up to 3 dB noise reduction on the advancing side and up to 2 dB on the retreating side. The corresponding vibration levels are compared to

Table 3: Simultaneous vibration and noise reduction obtained using the five microflap configuration for various values of the relative weighting parameter W_α.

W_α	% change in 4/rev vertical hub shear	dB change in right rear skid noise
0.1	55	-6.4
0.2	55	-6.2
0.3	42	-6.2
0.4	-2	-5.7
0.5	-16	-4.8
0.6	-25	-3.6
0.7	-55	-2.5
0.8	-56	-2.1
0.9	-64	-1.7

the baseline levels in Fig. 11. The dual and five microflap configurations yield 34% and 55% reduction in the 4/rev vertical hub shear, respectively. This clearly demonstrates that simultaneous reduction of vibrations and noise is feasible using microflaps. Microflap deflection histories over one complete revolution during simultaneous reduction using the dual and five microflap configurations are shown in Fig. 12. Microflap numbering for the five microflap configuration begins from the inboard microflap, i.e. 'Flap1' in the legend refers to the inboard microflap and 'Flap5' refers to the outboard microflap. It is interesting to note that the deflection histories for the outboard microflaps in both the configurations are predominantly 4/rev.

4.2 Comparison to a plain flap

Simultaneous vibration and noise reduction capabilities of the dual microflap configuration are compared to those of the dual plain flap configuration. The noise levels computed during simultaneous reduction using dual microflap and the dual plain flap are compared to the baseline levels in Fig. 13. On the advancing side, the dual plain flap yields up to 3 dB noise reduction whereas the dual microflap yields up to 2 dB. However, on the retreating side, the dual microflap configuration yields up to 2 dB noise reduction while the dual plain flap shows no effect. The vibration levels computed during simultaneous reduction using dual microflap and dual plain flap configurations are compared in Fig. 14. The dual plain flap yields up to 51 % reduction in the 4/rev vertical hub shear compared to 34% by the dual microflap. It is interesting to note that compared to the plain flap, the microflap demonstrates better effectiveness in reducing the noise levels over the entire carpet plane, i.e. both the advancing and the retreating sides, but yields less reduction in vibrations. This observation further illustrates the difficulty in simultaneously reducing vibrations and noise in helicopters. The dual microflap and dual plain flap deflection histories over one completer rotor revolution during simultaneous reduction are shown in Fig. 15. The deflection histories for the microflap and the plain flap show resemblance in the overall shape.

4.3 Effect of actuator saturation

To determine the effect of actuator saturation on the simultaneous vibration and noise reduction capabilities of the microflaps, the various saturation approaches described earlier were implemented for the case of a heavy BVI descending flight condition at advance ratio $\mu = 0.15$ and descent angle $\alpha_D = 6.5°$. The simulations are performed using the dual microflap configuration with $W_\alpha = 0.6$, see Table 2. The noise levels computed on the carpet plane during simultaneous reduction using the different saturation approaches are compared to the baseline noise levels in Fig. 16. The TR approach reduces the noise levels by 1 dB on both the advancing and retreating sides of the rotor disk. The SC, AW, and the OPT approaches yield similar performance with 2 dB noise reduction on both the advancing and retreating sides. The 4/rev vibratory hub loads obtained during simultaneous reduction using the various saturation approaches are compared to the baseline levels in Fig. 17. The TR and SC approaches result in a 29% and 9% *increase* in the vibration objective, respectively. The AW approach yields 23% reduction whereas the OPT approach yields a 29% reduction in the vibration objective. Significantly better performance obtained using the AW and OPT approaches is evident particularly in the vertical hub shear component. The TR and SC approaches reduce the vertical hub shear by 3% and 10%, respectively, whereas, the AW and OPT approaches reduce the vertical hub shear by 34% and 37%, respectively. Overall, the AW and OPT approaches yield similar simultaneous BVI noise and vibration reduction performance. However, the OPT approach requires significantly less computational time to converge taking only 10 control updates, 80 rotor revolutions, compared to over 100 control updates, 800 rotor revolutions, required for the AW approach.

The inboard and outboard microflap deflection histories corresponding to the various saturation approaches are shown in Fig. 18. In the AW approach, the maximum deflection of the inboard microflap is less than the saturation limit. This under-utilization of one of the microflaps is primarily a result of the fact that the same control weighting, c_{wu} in Eq. (32),

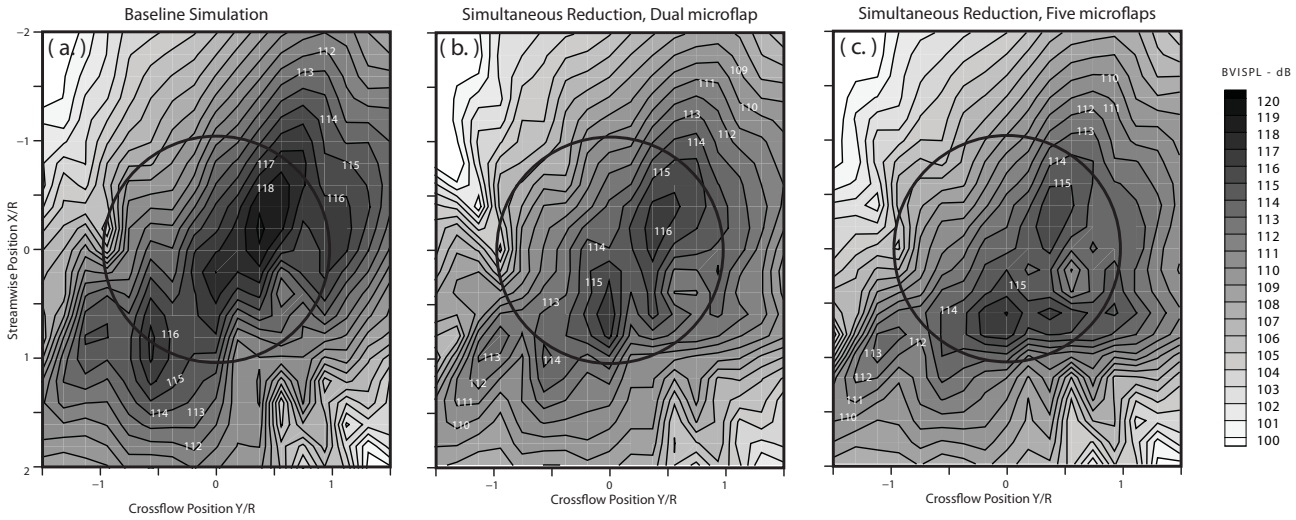

Figure 10: Noise levels computed on the carpet plane during simultaneous vibration and noise reduction using microflaps.

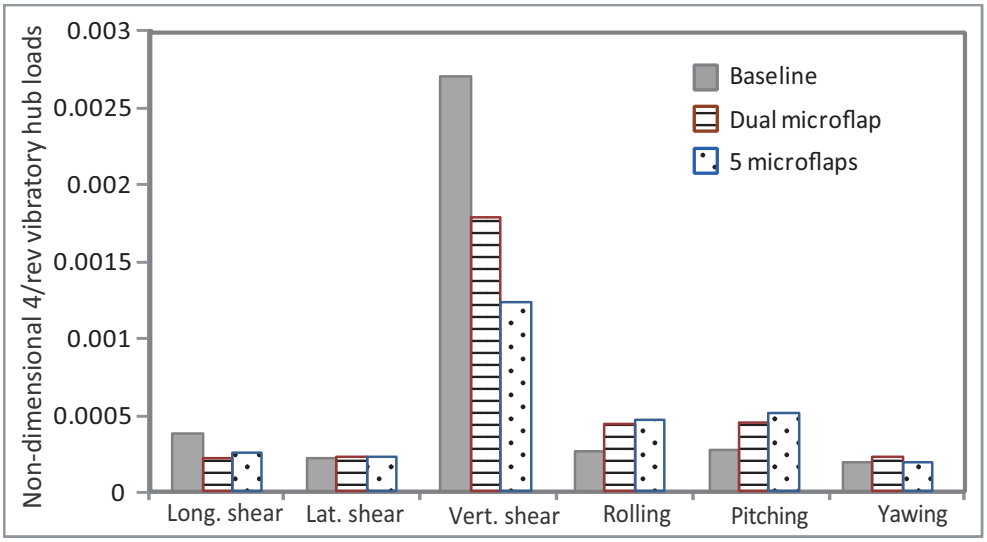

Figure 11: Vibration levels computed during simultaneous vibration and noise reduction using microflaps.

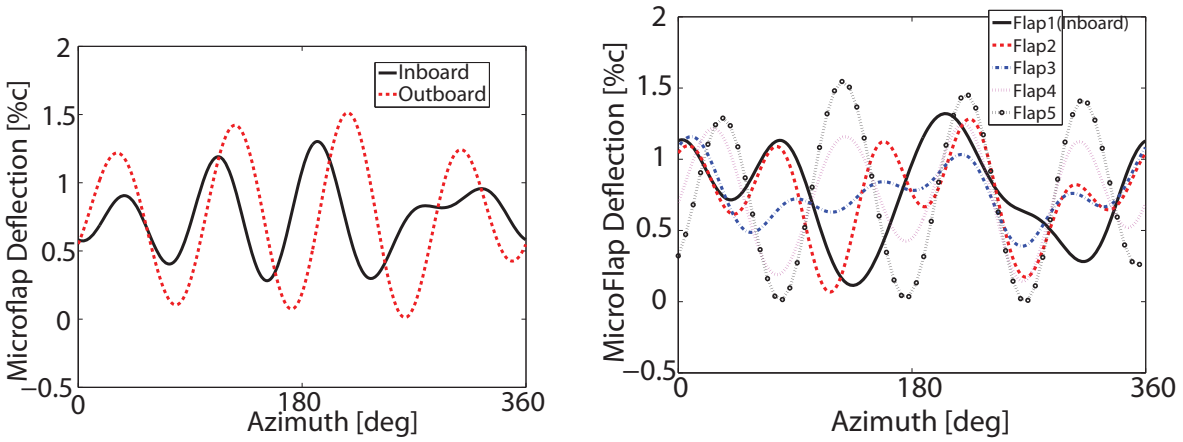

(a) Dual microflap

(b) Five microflaps

Figure 12: Microflap deflection histories over one complete revolution for the dual and five microflap configurations during simultaneous vibration and noise reduction.

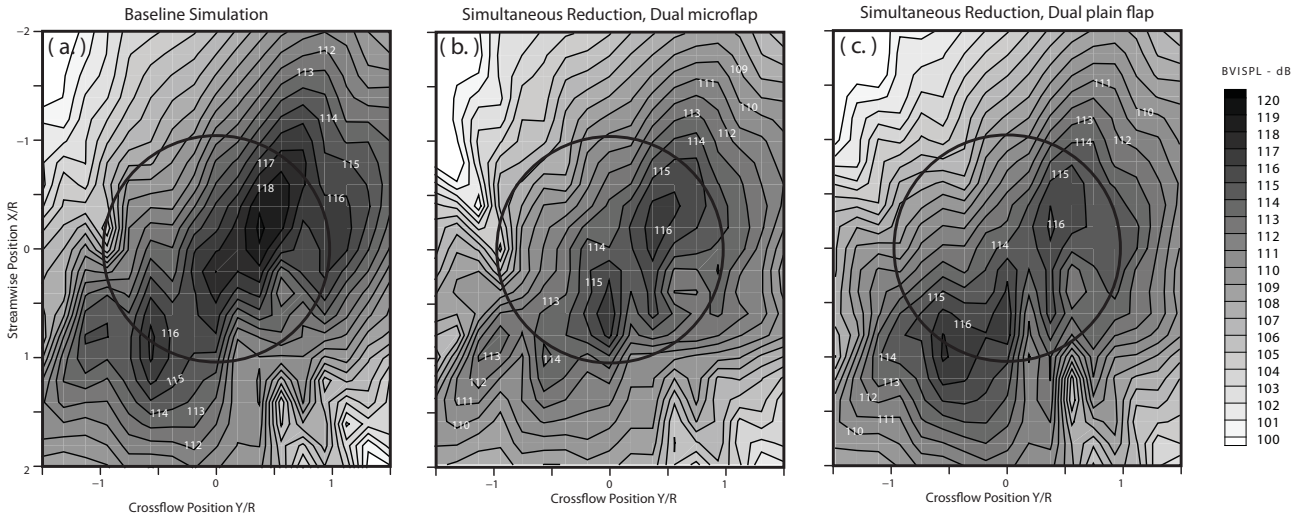

Figure 13: Comparison of the noise levels computed on the carpet plane during simultaneous vibration and noise reduction using a dual microflap and a dual plain flap.

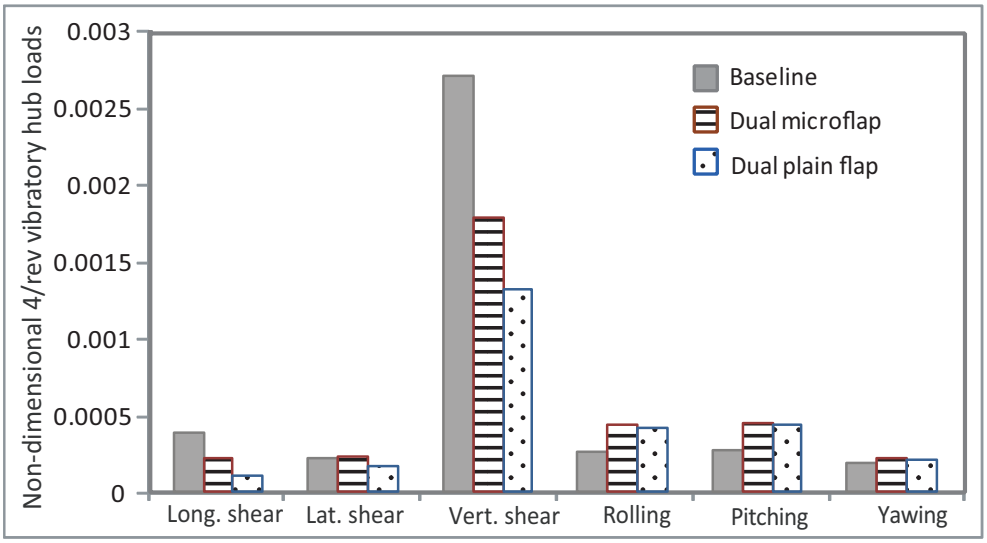

Figure 14: Comparison of the vibration levels computed during simultaneous vibration and noise reduction using a dual microflap and a dual plain flap.

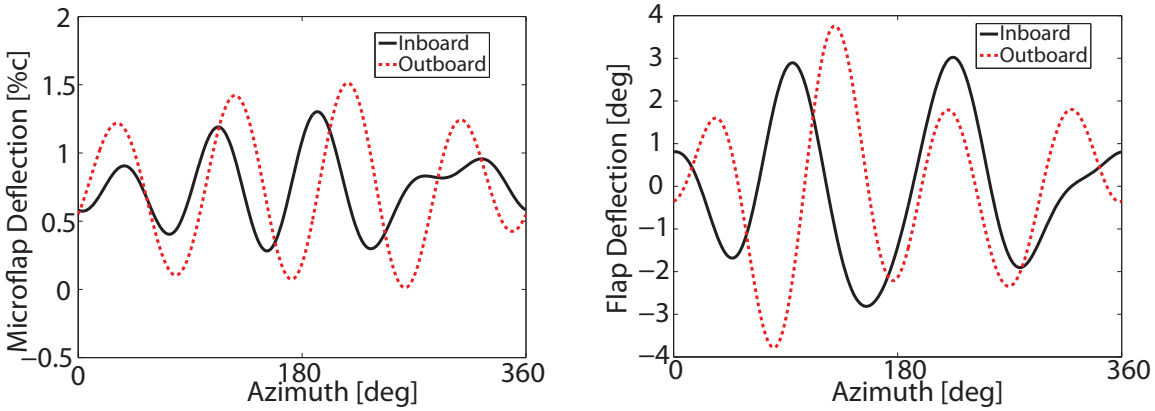

(a) Dual microflap

(b) Dual plain flap

Figure 15: Deflection histories over one complete revolution for the dual microflap and the dual plain flap configurations during simultaneous vibration and noise reduction.

is used for both the flaps. Using a different control weighting for the two microflaps results in a significant increase in the computational time. As is evident from the constraint inequalities in Eq. (34), the OPT approach optimizes the two microflaps individually, facilitating the use of both the microflaps to the maximum possible extent.

The effect of actuator saturation was also examined using the five microflap configuration and $W_\alpha = 0.7$ which, as shown in Table 3, yields an optimal reduction in the vertical hub shear and noise levels. The noise levels computed on the carpet plane during simultaneous reduction using the different saturation approaches are compared to the baseline noise levels in Fig. 19. The TR approach reduces the noise levels by 1 dB on both the advancing and retreating sides of the rotor disk. The SC approach results in a 2 dB noise reduction on both the advancing and the retreating sides. The AW approach yields a 3 dB reduction on the advancing side and a 2 dB reduction on the retreating side. The OPT approach yields the best performance with a 4 dB noise reduction on the advancing side and a 3 dB reduction on the retreating side. The 4/rev vibratory hub loads obtained during simultaneous reduction using the various saturation approaches are compared to the baseline levels in Fig. 20. The TR approach reduces the vertical hub shear by 23%. The SC approach causes a 7% increase in the vertical hub shear. The AW and OPT approaches reduce the vertical hub shear by 55% and 49%, respectively. Overall, OPT approach yields the best performance in simultaneously reducing the BVI noise and vibration.

The microflap deflection histories corresponding to the various saturation approaches are shown in Fig. 21. In the AW approach, the maximum deflection of the inboard microflaps is less than the saturation limit, whereas the OPT approach utilizes all the microflaps to the maximum possible extent.

Vibration reduction performance of the various saturation approaches is also compared at a high speed level flight condition with $\mu = 0.3$. Vibratory hub loads obtained from the different saturation approaches for the dual microflap configuration are shown in Fig. 22. The TR and SC approaches yield 25% and 28% reductions in the vibration objective, respectively. However, both of them cause a small increase in the vertical hub shear. The AW and the OPT approaches yield exceptional performance with 94% and 98% reductions in the vibration objective, respectively. The microflap deflection histories corresponding to the various saturation approaches are shown in Fig. 23. The AW approach significantly under-utilizes the outboard microflap whereas the OPT approach utilizes both microflaps to the maximum possible extent.

5 An Alternative Approach to Simultaneous Vibration and Noise Reduction

It is evident from the results presented in this paper as well as experimental results obtained on vibration and noise reduction in full scale wind tunnel tests that simultaneous reduction of vibration and noise is a challenging goal. These two objective functions impose conflicting demands on the controller and the pareto optimal solution obtained represents a compromise that is not completely satisfactory. Therefore, a fundamental question to be addressed is whether there are viable alternatives to on blade control implementation with multiple objectives.

An interesting alternative for vibration control has been developed and bench tested by a partnership between Sikorsky Aircraft Co. and the LORD Co [36, 37]. The system consists of two primary components:

1. A dual frequency Hub Mounted Vibration Suppressor (HMVS) which is mounted on the hub and operates in the rotating system, and its purpose is to eliminate the in-plane vibratory hub loads (F_x,F_y), and

2. An Active Vibration Control (AVC) system that consists of actuators placed around the gearbox, and operates in the fixed non-rotating fuselage system. The role of the AVC actuators is to reduce (nullify) the other large components of vibration (F_z,M_x,M_y). Thus the combined system is capable of suppressing all the significant oscillatory loads from the main rotor.

This system was bench tested in a LORD test facility on a CH-3 fuselage [36]. The rotating part of the system was attached to a large steel plate on the top of the CH-3 fuselage that was resting on wheels. The HMVS system was combined with a fuselage based AVC system consisting of two pairs of actuators. A single centralized controller provided simultaneous control commands to both the HMVS and the fixed system AVC units based upon vibration measurements obtained from vibration control accelerometers. The control commands were provided directly to the AVC actuator, and separately to the HMVS unit via a slip-ring assembly, which was also used to provide power to the HMVS system.

Simulated disturbance loads were introduced to the test rig by disturbance actuators located in the fixed system below the HMVS. The disturbance actuators introduced 4/rev components F_x,F_y,F_z,M_x andM_Y corresponding to a 4/rev frequency of 17.2 Hz. The performance of this combination of actuators, partially in the rotating system and partially

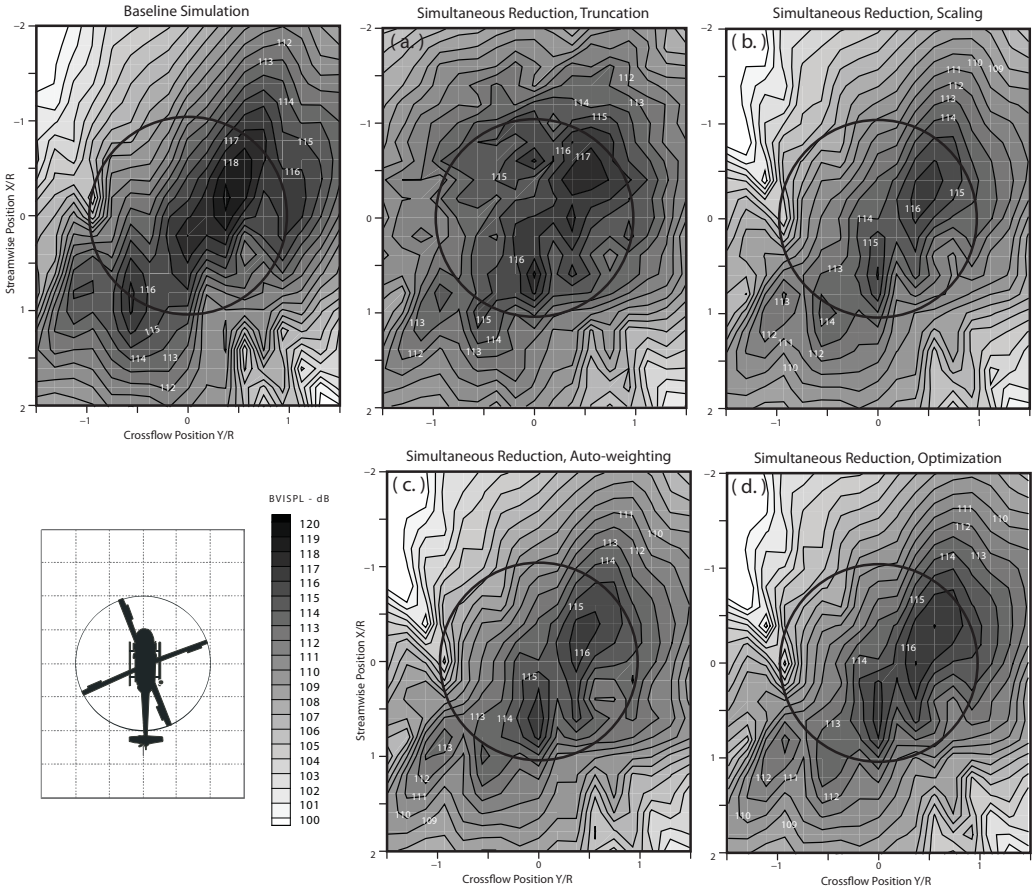

Figure 16: Reduction in noise levels obtained during simultaneous BVI noise and vibration reduction using the various saturation approaches for the dual microflap configuration at a heavy BVI descending flight condition with $\mu = 0.15$.

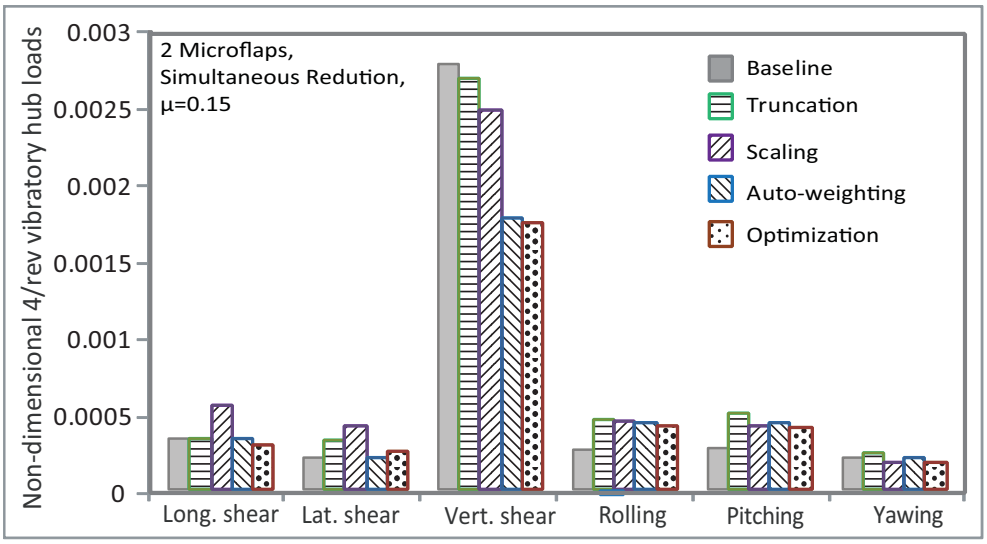

Figure 17: Reduction in 4/rev vibratory hub shears and moments obtained during simultaneous BVI noise and vibration reduction using the various saturation approaches for the dual microflap configuration at a heavy BVI descending flight condition with $\mu = 0.15$.

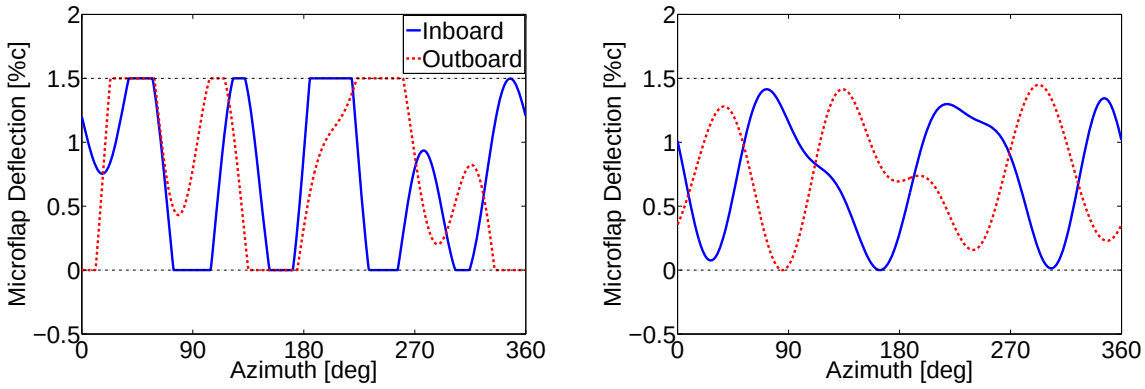

(a) Truncation

(b) Scaling

(c) Auto-weighting

(d) Optimization

Figure 18: Dual microflap deflection histories corresponding to the various saturation approaches at a heavy BVI descending flight condition with $\mu = 0.15$.

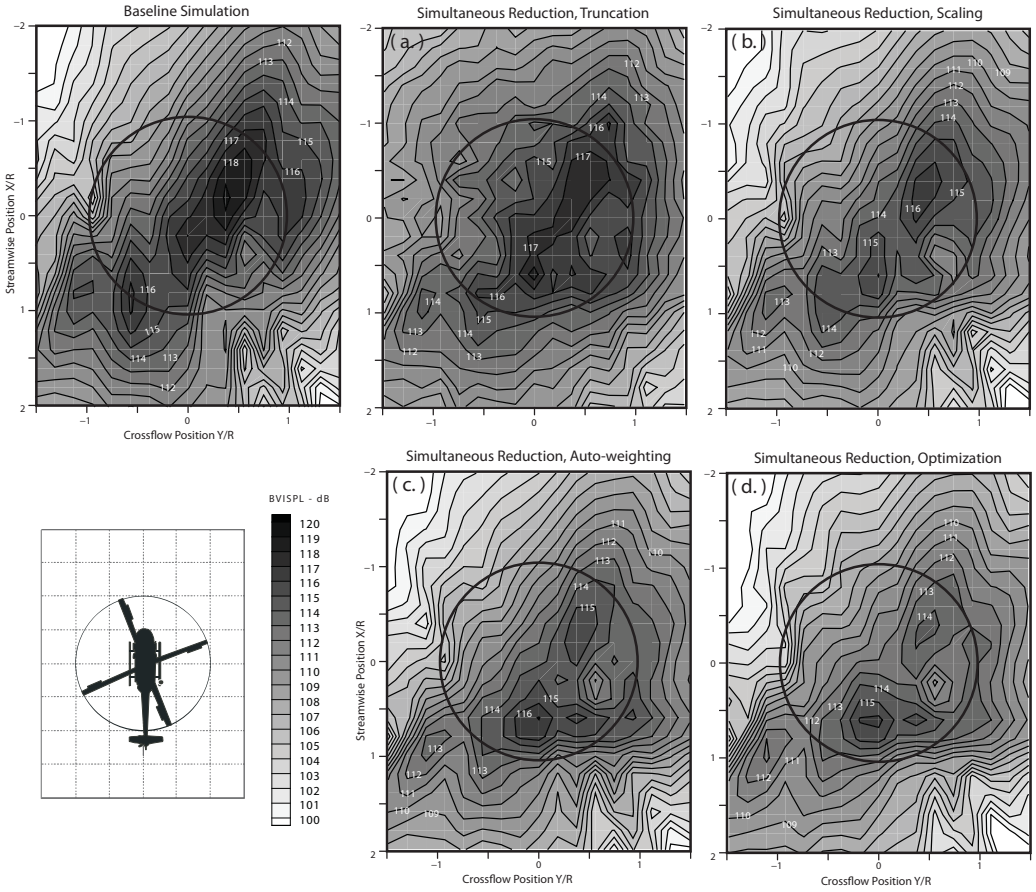

Figure 19: Reduction in noise levels obtained during simultaneous BVI noise and vibration reduction using the various saturation approaches for the five microflap configuration at a heavy BVI descending flight condition with $\mu = 0.15$.

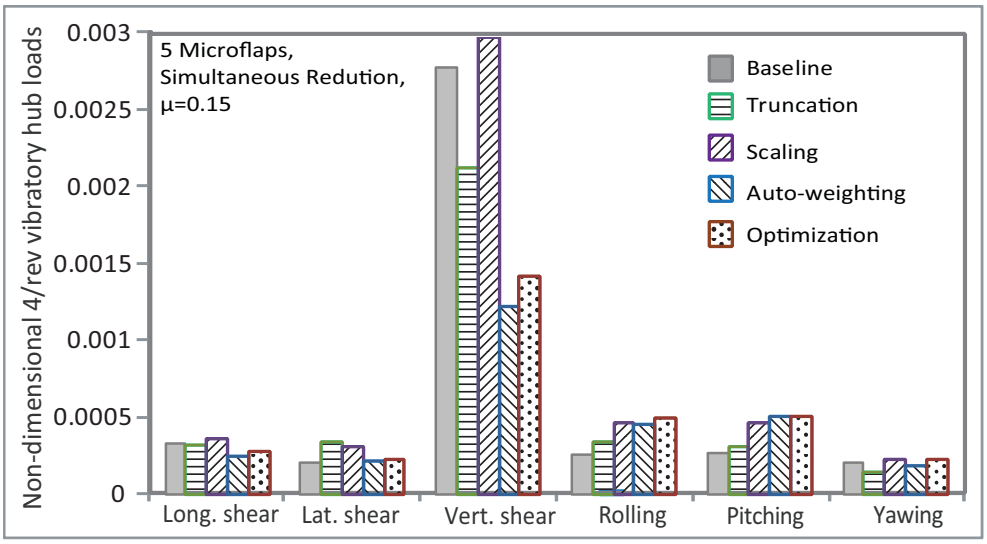

Figure 20: Reduction in 4/rev vibratory hub shears and moments obtained during simultaneous BVI noise and vibration reduction using the various saturation approaches for the five microflap configuration at a heavy BVI descending flight condition with $\mu = 0.15$.

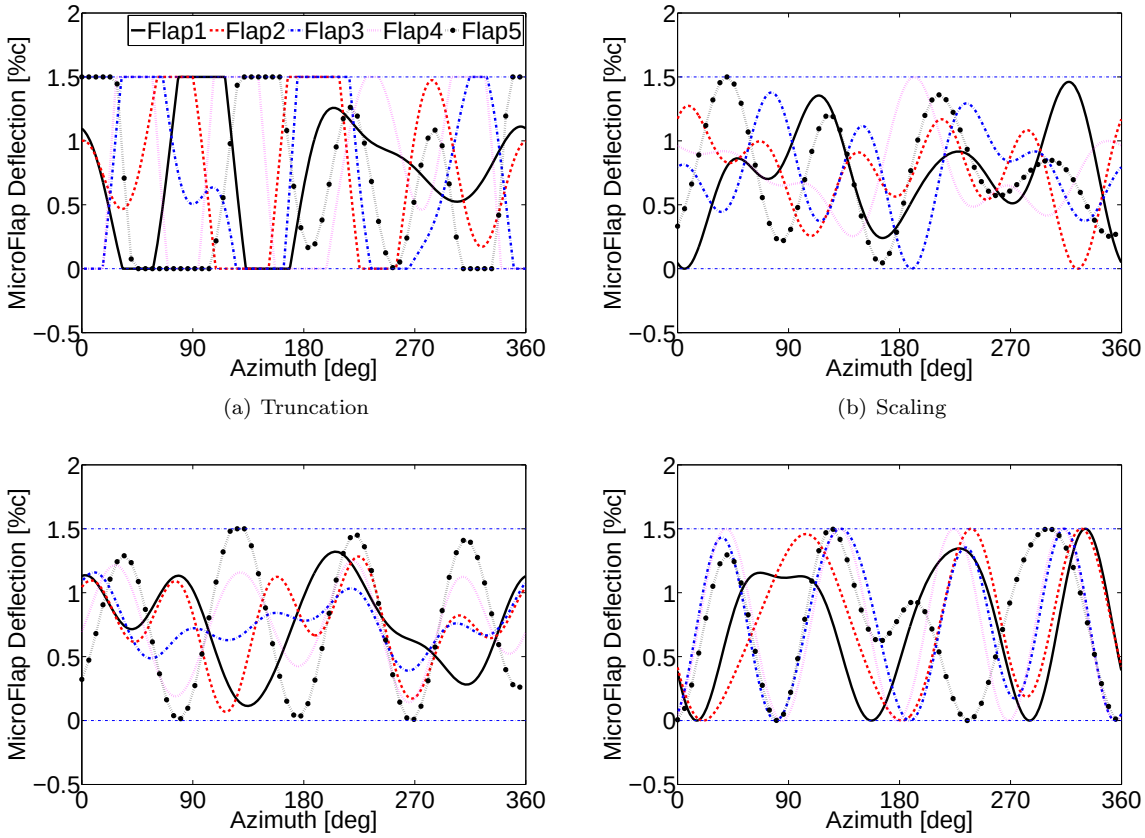

(a) Truncation

(b) Scaling

(c) Auto-weighting

(d) Optimization

Figure 21: Segmented five microflap deflection histories corresponding to the various saturation approaches at a heavy BVI descending flight condition with $\mu = 0.15$. 'Flap1' in the legend refers to the inboard microflap and 'Flap5' refers to the outboard microflap.

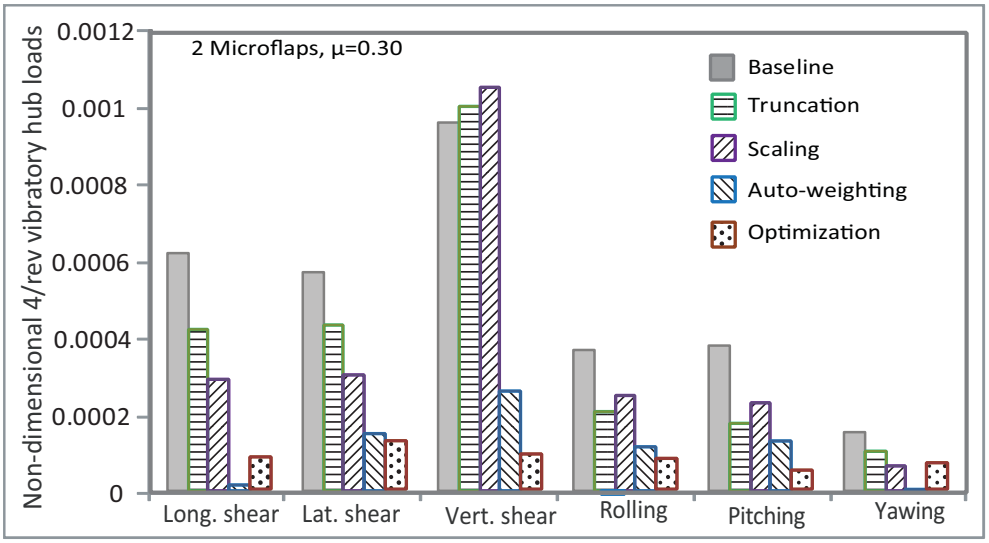

Figure 22: Reduction in 4/rev vibratory hub shears and moments obtained using the various saturation approaches for the dual microflap configuration at a high-speed flight condition with $\mu = 0.3$.

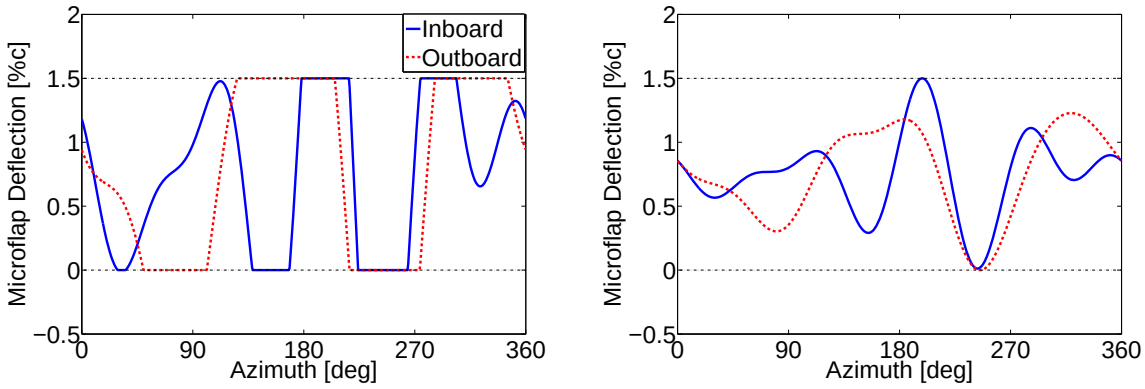

(a) Truncation

(b) Scaling

(c) Auto-weighting

(d) Optimization

Figure 23: Dual microflap deflection histories corresponding to the various saturation approaches at a high-speed flight condition with $\mu = 0.3$.

in the fixed system, produced good vibration control during simulated steady forward flight. The performance during simulated maneuver conditions was considerably worse. In both cases the need for an improved control algorithm was mentioned, however the actual control algorithm used during the bench test was not specified.

The relative success of this system implies that for simultaneous vibration and noise reduction, a hybrid system, consisting of a combined HMVS and AVC system for vibration reduction, and an on blade controller based on active flap or microflaps may represent the best solution. Since the combined HMVS and AVC system are limited strictly to vibration reduction, it is clear that the appropriate objective functions for the on blade controller should consist of either noise reduction or performance enhancement. Furthermore, since the vibration control system that is described here already has a slip-ring assembly, it is suitable for transferring control commands and power to both systems. The modeling, analysis and simulation of such a system should be undertaken.

6 Summary and Conclusions

The effectiveness of two sliding microflap configurations, with a height of 1.5% of blade chord, were examined for simultaneous vibration and noise reduction under heavy BVI conditions in descending flight at $\mu = 0.15$. The first was a dual microflap configuration, and the second one was a five microflap configuration shown in Fig. 7. The performance of the microflaps were also compared to a dual plain flap configuration, illustrated in Fig. 9. A saturation control algorithm was developed for limiting the microflap or flap deflections that yields the best utilization of on blade controllers implemented through multiple control surfaces. The principal conclusions of the study are summarized below.

1. For simultaneous BVI vibration and noise reduction the dual microflap configuration yields 2 dB noise reduction on both the advancing and the retreating sides while simultaneously reducing the 4/rev vibratory vertical hub shear magnitude by 34%.

2. The five microflap configuration yields 3 dB noise reduction on the advancing side and 2 dB reduction on the retreating side while simultaneously reducing the 4/rev vibratory vertical hub shear magnitude by 55%.

3. Simultaneous vibration and noise reduction capabilities of the dual microflap were compared to that of a dual 20%c plain flap configuration. On the advancing side, the dual plain flap yields 3 dB noise reduction compared to 2 dB by the dual microflap. However, the dual plain flap does not yield any reduction on the retreating side whereas the dual microflap yields up to 2 dB reduction.

4. The dual plain flap reduces the 4/rev vibratory hub shear by 51% compared to 34% by the dual microflap. Interestingly, the microflap is more effective in reducing the noise over the entire carpet plane (both the advancing and the retreating sides). By comparison the plain flap is more effective in reducing vibrations.

5. The effect of actuator saturation on the performance of the HHC control algorithm was examined for several saturation approaches and it was found that the truncation and scaling approaches for limiting control surface deflection produced inconsistent and marginal results and should be avoided.

6. The auto-weighting and the optimization approaches were compared and both displayed very good performance. However, the optimization approach requires significantly less computer time and in the case of multiple control surfaces, it utilizes all of them to the maximum possible extent resulting thus producing superior performance.

7. The alternative approach described in Section 5, indicates that a Hub Mounted Vibration Suppressor operating jointly with Active Vibration Controllers in the fixed system is very effective for vibration reduction. On the other hand, on-blade control is effective for noise reduction. Therefore, a hybrid system combining these two ingredients might provide the best solution to simultaneous vibration and noise reduction.

Clearly, these conclusions demonstrate the effectiveness and control authority of the microflap for simultaneous BVI noise and vibration control in rotorcraft and establish the microflap as a viable active device for on-blade rotor control.

Acknowledgments

This research was supported by the Vertical Lift Research Center of Excellence (VLRCOE) sponsored by NRTC and U.S. Army with Dr. M. Rutkowski as grant monitor.

REFERENCES

1. Friedmann, P. P. and Millott, T. A. , "Vibration Reduction in Rotorcraft Using Active Control: A Comparison of Various Approaches," Journal of Guidance, Control, and Dynamics, Vol. 18, (4), July-August 1995, pp. 664–673.

2. Splettstoesser, W. , Kube, R. , Wagner, W. , Seelhorst, U. , Boutier, A. , Micheli, F. , Mercker, E. , and Pengel, K. , "Key Results From a Higher Harmonic Control Aeroacoustic Rotor Test (HART)," Journal of the American Helicopter Society, Vol. 42, (1), January 1997, pp. 58–78.

3. Swanson, S. M. , Jacklin, S. A. , Blaas, A. , Niesl, G. , and Kube, R. , "Reduction of Helicopter BVI Noise, Vibration, and Power Consumption through Individual Blade Control," Proceedings of the 51st Annual Forum of the American Helicopter Society, Fort Worth, TX, May 1995, pp. 662–680.

4. Jacklin, S. A. , Haber, A. , de Simone, G. , Norman, T. , Kitaplioglu, C. , and Shinoda, P. , "Full-Scale Wind Tunnel Test of an Individual Blade Control System for a UH-60 Helicopter," Proceedings of the 51st Annual Forum of the American Helicopter Society, Montreal, Canada, June 2002.

5. Patt, D. , Liu, L. , and Friedmann, P. P. , "Simultaneous Vibration and Noise Reduction in Rotorcraft Using Aeroelastic Simulation," Journal of the American Helicopter Society, Vol. 51, (2), April 2006, pp. 127–140.

6. Koratkar, N. A. and Chopra, I. , "Wind Tunnel Testing of a Smart Rotor Model with Trailing Edge Flaps," Journal of the American Helicopter Society, Vol. 47, (4), October 2002, pp. 263–272.

7. Straub, F. K. , Anand, V. , Birchette, T. S. , and Lau, B. H. , "Wind Tunnel Test of the SMART Active Flap Rotor," Proceedings of the 65th American Helicopter Society Annual Forum, Grapevine,TX, May 2009.

8. Liu, L. , Padthe, A. K. , and Friedmann, P. P. , "A Computational Study of Microflaps with Application to Vibration Reduction in Helicopter Rotors," AIAA Journal, Vol. 49, (7), July 2011, pp. 1450–1465.

9. Min, B. Y. , Sankar, L. , and Bauchau, O. A. , "A CFD-CSD Coupled Analysis of Hart II Rotor Vibration Reduction Using Gurney Flaps," Proceedings of the 66th American Helicopter Society Annual Forum, Phoenix, AZ, May 11-13 2010.

10. Padthe, A. K. and Friedmann, P. P. , "Simultaneous BVI Noise and Vibration Reduction in Rotorcraft Using Microflaps Including the Effect of Actuator Saturation," Proceedings of the 68th American Helicopter Society Annual Forum, Fort Worth, TX, May 2012.

11. Padthe, A. K. and Friedmann, P. P. , "Actuator Saturation in Individual Blade Control of Rotorcraft," Proceedings of the 53rd AIAA/ASME/ASCE/AHS/ACS Structures, Structural Dynamics and Materials Conference, Honolulu,HI, April 2012.

12. Liebeck, R. H. , "Design of Subsonic Airfoils for High Lift," Journal of Aircraft, Vol. 15, (9), Sept 1978, pp. 547–561.

13. Storms, B. L. and Jang, C. S. , "Lift Enhancement of an Airfoil Using a Gurney Flap and Vortex Generators," Journal of Aircraft, Vol. 31, (3), May-June 1994, pp. 542–547.

14. Baker, J. P. , Standish, K. J. , and van Dam, C. P. , "Two-Dimensional Wind Tunnel and Computational Investigation of a Microtab Modified Airfoil," Journal of Aircraft, Vol. 44, (2), March-April 2007, pp. 563–572.

15. Maughmer, M. D. and Bramesfeld, G. , "Experimental Investigation of Gurney Flaps," Journal of Aircraft, Vol. 45, (6), November-December 2008, pp. 2062–2067.

16. Chow, R. and van Dam, C. P. , "Unsteady Computational Investigations of Deploying Load Control Microtabs," Journal of Aircraft, Vol. 43, (5), Sept-Oct 2006, pp. 641–648.

17. Lee, H.-T. , Kroo, I. M. , and Bieniawski, S. , "Flutter Suppression for High Aspect Ratio Flexible Wings Using Microflaps," Proceedings of the 43rd AIAA/ASME/ASCE/AHS/ACS Structures, Structural Dynamics and Materials Conference, Reno, NV, Apr 2002. AIAA Paper No. 2002-1717.

18. Matalanis, C. G. and Eaton, J. K. , "Wake Vortex Alleviation Using Rapidly Actuated Segmented Gurney Flaps," AIAA Journal, Vol. 45, (8), August 2007, pp. 1874–1884.

19. Nikolic, V. R. , "Two Aspects of the Use of Full- and Partial-Span Gurney Flaps," Journal of Aircraft, Vol. 44, (5), Sept-Oct 2007, pp. 1745–1748.

20. Nakafuji, D. T. Y. , van Dam, C. P. , Smith, R. L. , and Collins, S. D. , "Active Load Control for Airfoils using Microtabs," Journal of Solar Energy Engineering, Vol. 123, (4), November 2001, pp. 282–289.

21. Kinzel, M. P. , Maughmer, M. D. , and Lesieutre, G. L. , "Miniature Trailing-Edge Effectors for Rotorcraft Performance Enhancement," Journal of the American Helicopter Society, Vol. 52, (2), April 2007, pp. 146–158.

22. Kinzel, M. P. , Maughmer, M. D. , and Duque, E. P. N. , "Numerical Investigation on the Aerodynamics of Oscillating Airfoils with Deployable Gurney Flaps," AIAA Journal, Vol. 48, (7), July 2010, pp. 1457–1469.

23. Patt, D. , Liu, L. , Chandrasekar, J. , Bernstein, D. S. , and Friedmann, P. P. , "Higher-Harmonic-Control Algorithm for Helicopter Vibration Reduction Revisited," Journal of Guidance, Control, and Dynamics, Vol. 28, (5), September-October 2005, pp. 918–930.

24. Rogers, K. L. , Airplane Math Modeling Methods for Actively Control Design. AGARD-CP-228, August 1977.

25. Myrtle, T. F. and Friedmann, P. P. , "Application of a New Compressible Time Domain Aerodynamic Model to Vibration Reduction in Helicopters Using an Actively Controlled Flap," Journal of the American Helicopter Society, Vol. 46, (1), January 2001, pp. 32–43.

26. Liu, L. , Padthe, A. , Friedmann, P. P. , Quon, E. , and Smith, M. , "Unsteady Aerodynamics of an Airfoil/Flap Combination on a Helicopter Rotor Using CFD and Approximate Methods," Journal of American Helicopter Society, Vol. 56, (3), July 2011, pp. 1–13.

27. Peroomian, O. , Chakravarthy, S. , Palaniswamy, S. , and Goldberg, U. , "Convergence Acceleration for Unified-Grid Formulation Using Preconditioned Implicit Relaxation," AIAA Paper 98-0116, Reno, NV, January 1998.

28. Peroomian, O. , Chakravarthy, S. , and Goldberg, U. , "A "Grid-Transparent" Methodology for CFD," AIAA Paper 97-0724, Reno, NV, January 1997.

29. Glaz, B. , Friedmann, P. P. , Liu, L. , Kumar, D. , and Cesnik, C. E. S. , "The AVINOR Aeroelastic Simulation Code and Its Application to Reduced Vibration Composite Rotor Blade Design," Proceedings of the 50th AIAA/ASME/ASCE/AHS/ACS Structures, Structural Dynamics and Materials Conference, Palm Springs, CA, May 2009. AIAA Paper No. 2009-2601.

30. Brentner, K. , A Computer Program Incorporating Realistic Blade Motions and Advanced Acoustic Formulation. NASA Technical Memorandum, Vol. 87721 1986.

31. Patt, D. , Liu, L. , and Friedmann, P. P. , "Rotorcraft Vibration Reduction and Noise Prediction Using a Unified Aeroelastic Response Simulation," Journal of the American Helicopter Society, Vol. 50, (1), January 2005, pp. 95–106.

32. Abbott, I. H. , Doenhoff, A. E. V. , and Stivers, L. S. , Summary of Airfoil Data. NACA Report 824, 1945.

33. Fletcher, R. , *Practical Methods of Optimization*, John Wiley and Sons, 1987.

34. Schittkowski, K. , "NLQPL: A FORTRAN-Subroutine Solving Constrained Nonlinear Programming Problems," Annals of Operations Research, Vol. 5, 1985, pp. 485–500.

35. Padthe, A. K. , Liu, L. , and Friedmann, P. P. , "Numerical Evaluation of Microflaps for On Blade Control of Noise and Vibration," Proceedings of the 52nd AIAA/ASME/ASCE/AHS/ACS Structures, Structural Dynamics and Materials Conference, Denver, CO, April 2011.

36. Brigley, M. , Welsh, W. , Altieri, R. , and Rich, A. , "Design and Testing of a New Vibration Suppression System," Proceedings of the 67th American Helicopter Society Annual Forum, Virginia Beach, VA, May 2011.

37. Wilson, M. and Jolly, M. , "Ground Test of a Hub Mounted Active Vibration Suppressor," Proceedings of the 63rd American Helicopter Society Annual Forum, Virginia Beach, VA, May 2007.